White Rose Research Online

eprints@whiterose.ac.uk
https://eprints.whiterose.ac.uk
Universities of Leeds, Sheffield and York

Deposited via The University of Sheffield.

White Rose Research Online URL for this paper:
https://eprints.whiterose.ac.uk/id/eprint/139345/

Version: Accepted Version

Article:
Wu, Z.Z., Zhu, Z.Q., Wang, C. et al. (2019) Reduction of open-circuit dc-winding-induced voltage in wound field switched flux machines by skewing. IEEE Transactions on Industrial Electronics, 66 (3). pp. 1715-1726. ISSN: 0278-0046

https://doi.org/10.1109/TIE.2018.2838106

© 2018 IEEE. Personal use of this material is permitted. Permission from IEEE must be obtained for all other users, including reprinting/ republishing this material for advertising or promotional purposes, creating new collective works for resale or redistribution to servers or lists, or reuse of any copyrighted components of this work in other works. Reproduced in accordance with the publisher's self-archiving policy.

Reuse
Items deposited in White Rose Research Online are protected by copyright, with all rights reserved unless indicated otherwise. They may be downloaded and/or printed for private study, or other acts as permitted by national copyright laws. The publisher or other rights holders may allow further reproduction and re-use of the full text version. This is indicated by the licence information on the White Rose Research Online record for the item.

Takedown
If you consider content in White Rose Research Online to be in breach of UK law, please notify us by emailing eprints@whiterose.ac.uk including the URL of the record and the reason for the withdrawal request.

UNIVERSITY OF LEEDS
University of Sheffield
UNIVERSITY of York

Reduction of Open-Circuit DC Winding Induced Voltage in Wound Field Switched Flux Machines by Skewing

Z. Z. Wu, *Member, IEEE*, Z. Q. Zhu, *Fellow, IEEE*, C. Wang, J. C. Mipo, S. Personnaz, and P. Farah

***Abstract*—In this paper, the open-circuit DC winding induced voltage in a wound field switched flux (WFSFs) machines is analysed. The phenomenon of open-circuit DC winding induced voltage is illustrated and the mechanism is explained. Rotor skewing is proposed to reduce the open-circuit DC winding induced voltage, and the optimal skewing angle is analytically derived based on the analytically deduced harmonic orders of the open-circuit DC winding induced voltage. Finite element (FE) analyses show that the open-circuit DC winding induced voltages in the analysed 12-stator-pole partitioned stator WFSF machines having 10-, 11-, 13-, and 14-rotor-pole rotors can be effectively reduced by > 94%, whilst the AC winding phase fundamental back-EMFs can be maintained by > 95%. 12/10-stator/rotor-pole prototypes with skewed and non-skewed rotors are built and tested to verify the analytical and FE results.**

***Index Terms*—AC winding, DC winding, field winding, DC winding induced voltage, flux switching, open-circuit, skewing, step skewing, wound field switched flux machine.**

I. Introduction

DUE to the development of rare-earth permanent magnet (PM) material, electrical machines equipped with rare-earth PMs offer high torque density and efficiency and become the preferred designs in many applications from industrial drives to domestic appliances over recent years [1]. However, PM machines also suffer from some disadvantages, such as limited operating temperature, high price and pulsating of PMs, as well as relatively poor flux weakening characteristic. As pointed out in [2], non-PM machines are mainly made up of induction machine (IM) [3], switched reluctance machine (SRM) [4], and wound field (WF) synchronous machine including both the conventional wound-rotor synchronous machines with DC field winding placed in the rotor [5], and the wound field switched flux (WFSF) machines in which both the DC field and AC armature windings are accommodated in the stator [6]-[18]. Compared with IM and wound-rotor synchronous machines, both SRM and WFSF machines have a simple and robust rotor without winding, which is better for thermal dissipation, not to mention the brush and slip ring in the wound-rotor synchronous machines.

WFSF machines draw much attention recently [6]-[18]. Single phase WFSF machine designed for automotive applications is analyzed and presented in [6], with a compact and simple controller. Three-phase counterparts with various topologies are presented and analyzed in [11]-[18]. Prototypes for electric vehicles and traction applications are built and tested in [14] and [15], and the experimental results show that a WFSF machine has a similar torque capability as PM machines but features a lower cost. However, the DC field winding and the AC armature windings are overlapped in [11]-[15], which will cause longer end winding length and hence higher copper loss and lower efficiency.

To overcome the disadvantages caused by overlapped DC field winding and AC armature windings in [11]-[15], some efforts are made to put a DC field coil and an AC armature coil together in the same stator tooth with non-overlapping windings achieved, as studied in [16]. However, this type of WFSF machine suffers from lower torque density due to higher stator tooth magnetic saturation. A non-overlapping WFSF machine has a segmented or conventional rotor is proposed and analyzed in [17] and [18], respectively.

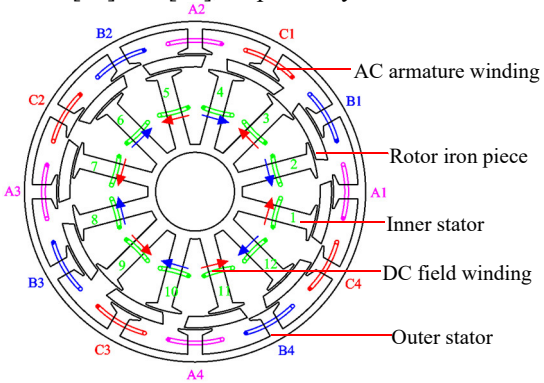

Fig. 1. Cross-section of a 12/10-stator/rotor-pole PS-WFSF machine.

However, the conventional WFSF machines [6]-[18] with

Manuscript received December 1, 2017; revised April 15, 2018; accepted May 2, 2018. *(Corresponding author: Z. Q. Zhu.)*

Z. Z. Wu, Z. Q. Zhu, and C. Wang are with the Electrical Machines and Drives Group, University of Sheffield, Sheffield, UK (wuzhongze@gmail.com, z.q.zhu@sheffield.ac.uk, cwang55@sheffield.ac.uk).

J. C. Mipo, S. Personnaz, and P. Farah are with Valeo Powertrain Electric Systems, 94017 Créteil Cedex, France (jean-claude.mipo@valeo.com, sophie.personnaz@valeo.com, philippe.farah@valeo.com).

single stator having both DC field and AC armature windings in the single stator suffer from the geometric area conflict between DC and AC windings and hence lower torque density, whilst the machine inner space is not fully utilized, not to mention the disadvantages caused by overlapping windings in some WFSF machines. In [19], a partitioned stator (PS) WFSF (PS-WFSF) machine in which DC field and AC armature windings are separately placed in the inner and outer stators is proposed, *e.g.* a 12/10-stator/rotor-pole PS-WFSF machine shown in Fig. 1. Compared with the conventional WFSF machines with single stator [11], PS-WFSF machines with double stators can exhibit more than 19% higher torque density due to the higher total area of DC and AC windings.

In [20], a 67kW PS-WFSM is designed and analyzed for electric vehicles. Finite element (FE) results show that the PS-WFSM can achieve a similar torque per unit volume as the Toyota Prius 2010 interior PM (IPM) machine [21], as shown in TABLE I, due to the concentrated winding and hence a shorter end winding height h_e. However, when the machine operates at open-circuit condition and the DC winding is supplied by a rated constant current I_f=16.3A, i.e. the DC winding copper loss is 3000W, a voltage pulsation is induced in the DC winding, of which the peak-to-peak value is 622.5V, i.e. 337.5% of the DC winding resistance voltage drop, as shown in Fig. 2.

TABLE I

PERFORMANCE COMPARISON BETWEEN TOYOTA PRIUS 2010 IPM MACHINE [21] AND PS-WFSM [20]

Item	Unit	IPM	PS-WFSM
Rated speed, Ω_r	rpm	2795	4000
Rated torque, T_r	Nm	205	160
Rated power, P_r	kW	60	67
Stack length, l_s	mm	50.8	183.26
Single side end winding height, h_e	mm	35(29)	18.37
Axial length with end winding, l_a	mm	114.8	220
Stator outer radius, R_o	mm	132	83
Machine volume without casing and cooling system, V	L	6.28	4.8
Rated torque per unit volume, TPV	Nm/L	32.62	33.6
Rated power per unit volume, PPV	kW/L	9.55	14.1

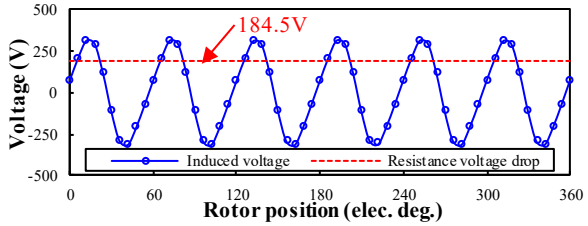

Fig. 2. Open-circuit DC winding induced voltage at rated rotor speed 4000rpm and DC winding resistance voltage drop of the 12/10-pole PS-WFSF machine in [20].

As a voltage perturbation to the DC winding voltage supply, the induced voltage in the DC winding will cause DC winding current ripple [17], [22]. In [22], the DC winding flux-linkage in a single phase WFSF machine having double rotors designed for rooftop wind power generation is modelled. In [17], the tested DC current peak-to-peak value is 19% of the average value when the prototype is operating at 500rpm. It is expected that the influence of DC winding induced voltage on the DC winding current ripple is similar with various rotor speeds, since both the DC winding induced voltage and the reactance are proportional to the rotor speed. However, the DC winding induced voltage will also challenge the DC power source and deteriorate the control performance in two aspects, when the DC winding excitation is controllable and realized by a half or a full H-bridge [13]. On one hand, the DC winding bus voltage needs to be higher than the DC winding resistance voltage drop to balance the DC winding induced voltage. On the other hand, a reverse output voltage from converter is required to balance the DC winding induced voltage negative value. As the half H-bridge cannot achieve this function, only the full H-bridge with a higher cost can be adopted.

TABLE II

KEY PARAMETERS OF 12-STATOR-POLE PS-WFSF MACHINES WITH 10-, 11-, 13- AND 14-ROTOR-POLE ROTORS

Items	Unit	12-stator-pole PS-WFSF machines			
Rotor pole number, N_r	-	10	11	13	14
Active axial length, L_{axial}	mm	50			
Outer radius of outer stator, R_{oso}	mm	45			
Inner radius of inner stator, R_{isi}	mm	10.4			
Width of outer air-gap, g_o	mm	0.5			
Width of inner air-gap, g_i	mm	0.5			
Length of outer stator tip top, l_{ott}	mm	0.5			
Length of outer stator tip bottom, l_{otb}	mm	1.5			
Length of inner stator tip top, l_{itt}	mm	0.5			
Length of inner stator tip bottom, l_{itb}	mm	1.5			
Yoke radius of outer stator, R_{osy}	mm	43	43	43	43.5
Inner radius of outer stator, R_{osi}	mm	36.5	36	36	36.5
Radius of rotor inner surface, R_{ri}	mm	33	33	33	34
Yoke radius of inner stator, R_{isy}	mm	12.5	12.5	12.5	12.5
Arc of outer stator tooth, θ_{ost}	°	6	6	6	5
Arc of outer stator tip, θ_{ot}	°	4	4	4	3
Arc of rotor piece outer edge, θ_{ro}	°	27	25	20	19
Arc of rotor piece inner edge, θ_{ri}	°	24	24	22	20
Arc of inner stator tooth, θ_{ist}	°	7	7	7	7
Arc of inner stator tip, θ_{it}	°	5	4	3	3
Rated rotor mechanical speed, Ω_{mr}	rpm	400			
Rated DC winding copper loss, p_{cufr}	W	60			
Number of turns per DC coil, N_{fc}	-	90			
Rated DC winding current, I_{fr}	A	3.64	3.66	3.67	3.79
Rated AC windings copper loss, p_{cuar}	W	60			
Number of turns per AC coil, N_{ac}	-	18			
Rated AC windings phase RMS current, I_{rmsr}	A	15.24	15.81	15.81	16.30
Rated AC windings phase RMS back-EMF @400rpm, E_{rmsr}	V	4.08	4.22	4.26	4.36
Rated on-load average electromagnetic torque, T_{avgr}	Nm	2.93	2.79	3.05	3.02
Rated on-load average electromagnetic power @400rpm, P_{avgr}	W	122.53	127.87	133.46	138.24

DC winding induced voltage consists of two components due to the open-circuit and armature reaction, respectively. Based on the small-scale PS-WFSF machines, this paper aims to investigate the mechanism of the open-circuit DC winding induced voltage, i.e. the component due to armature reaction is not accounted, and the corresponding reduction method. The paper is organized as follows. In section II, the machine topology of the PS-WFSF machine is introduced. In section III, the phenomenon of the open-circuit DC winding induced voltage is illustrated and its mechanism is explained, based on a small-scale 12/10-pole PS-WFSF machine. In section IV, based on the analytical deduction of harmonic orders, rotor skewing is proposed to minimize the open-circuit DC winding induced voltage and the optimal skewing angle is analytically derived. Influence of skewing angle and step-skewing steps on the

open-circuit DC winding induced voltage are also investigated in section IV, together with the influence of skewing on the torque performance. In section V, the 12/10-pole small-scale prototypes with skewed and non-skewed rotors are built and tested to verify the analytical and FE results, followed by discussion and conclusion in section VI. Although the analysis and investigation in this paper is based on the small-scale PS-WFSF machine, it is worth noting that the fundamental knowledge including mechanism and reduction method in this paper is also applicable to the large-scale counterparts, e.g. the 67kW one in [20].

II. Machine Topology

There are three main components in the PS-WFSF machine shown in Fig. 1 for the 12/10-stator/rotor-pole counterpart, *i.e.* 12-pole outer stator wound by 3-phase non-overlapping concentrated AC armature winding, 12-pole non-overlapping concentrated inner stator wound by DC field winding, and a sandwiched 10-pole rotor consists of iron pieces. It is worth noting that although the PS-WFSF machine shown in Fig. 1 has two stators, it is different from the conventional double stator machines [23]. In the conventional double stator machines, both the outer and inner stator windings have the same air-gap field function, whilst in the PS-WFSF machine they perform AC armature field and DC field generation, respectively [19].

The dimensional parameters of the analysed 12/10-pole PS-WFSF machine are shown in TABLE II, which can be referred to Fig. 3. It is worth noting that the parameters from L_{axial} to l_{itb} are fixed, whilst the rest are globally optimized for the highest average electromagnetic torque under brushless AC (BLAC) mode with zero *d*-axis current control, *i.e.* i_d=0, with total copper loss p_{cu}=120W, *i.e.* armature copper loss p_{cua}=60W and field copper loss p_{cuf}=60W, respectively. The slot filling factors for both DC winding and AC windings are 0.5.

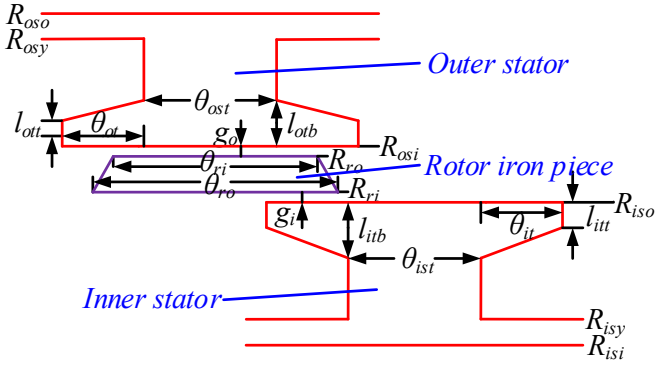

Fig. 3. Linear illustration of dimensional parameters.

III. Phenomenon and Mechanism of Open-Circuit Induced Voltage in DC Field Winding

A. Phenomenon

As well known, the DC winding current is desired to be constant in WFSM machines. This is also the ideal aim when the closed-loop DC winding current control is implemented. When the DC winding current is constant, the open-circuit DC winding flux-linkage in WF machines is always regarded as constant, and hence, there is no induced voltage for the DC winding according to Faraday's law. However, as shown in Fig. 4 for the 12/10-pole PS-WFSF machine, the open-circuit DC winding flux-linkage suffers from harmonics, *i.e.* 6th, 12th, 18th… As a consequence, voltage will be induced in the DC winding due to the variation of open-circuit DC winding flux-linkage ψ_f,

$$E_f = \frac{d(\psi_f)}{dt} = \frac{d(\psi_f)}{d(\theta_e)} \times \frac{d(\theta_e)}{d(\theta_t)} = \Omega_e \frac{d(\psi_f)}{d(\theta_e)} \quad (1)$$

where E_f is the open-circuit DC winding induced voltage. Ω_e is the rotor electric speed. θ_e is the rotor electric position.

Based on (1) and Fig. 4, the open-circuit DC winding induced voltage of the 12/10-pole PS-WFSF machine at Ω_m=400rpm can be illustrated in Fig. 5. When the rotor mechanical speed Ω_m=400rpm, the peak to peak value of the open-circuit DC winding induced voltage E_{pp}=2.10V, whilst the voltage drop of the DC winding resistance V_{Rf} is 16.47V. Consequently, the induced voltage ratio (IVR) of E_{pp} to V_{Rf} is 12.77%. IVR is defined as,

$$IVR = \frac{E_{pp}}{V_{Rf}} \times 100\% \quad (2)$$

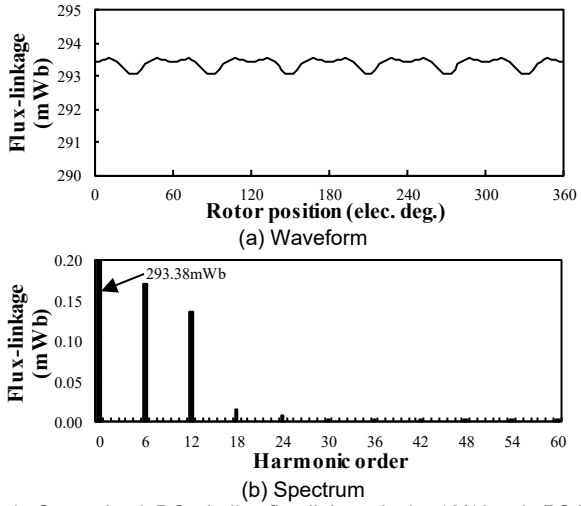

Fig. 4. Open-circuit DC winding flux-linkage in the 12/10-pole PS-WFSF machine (p_{cuf}=60W).

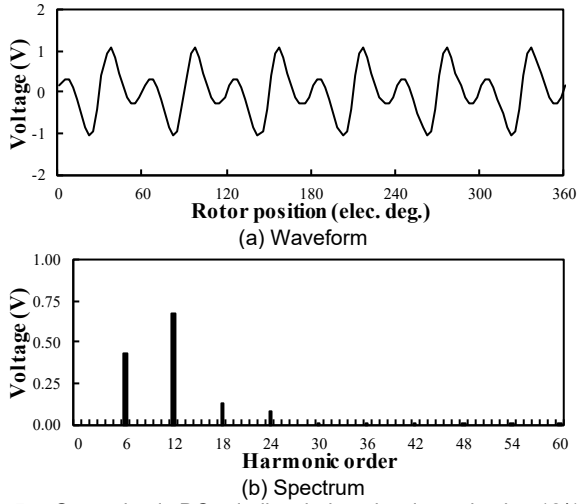

Fig. 5. Open-circuit DC winding induced voltage in the 12/10-pole PS-WFSF machine at 400rpm (p_{cuf}=60W).

Due to the existence of the DC winding induced voltage, the

DC winding voltage supply suffers from voltage perturbation caused by the induced voltage, which will cause challenge to the DC voltage controller and decrease the control performance, especially at high rotor speed since the induced voltage is proportional to the rotor speed. Therefore, it is necessary to investigate the mechanism of the open-circuit DC winding induced voltage and reduce it.

It is worth noting that IVR cannot be reduced by designing a lower DC coil turns N_{fc}, although E_{pp} will be lower. This can be explained as follows. E_{pp} can be expressed as,

$$E_{pp} = N_{fc} E_{pp1} \tag{3}$$

where E_{pp1} is the peak to peak value of the open-circuit DC winding induced voltage for each turn.

V_{Rf} can be expressed as,

$$V_{Rf} = I_f R_f = I_f \rho \frac{l_f}{s_f} = \frac{\rho I_f N_{fc}^2 l_{f1}}{S_f k_{pff}} \tag{4}$$

where I_f is the DC winding current. R_f is the DC winding resistance. ρ is the resistivity of DC winding. l_f is the DC winding length. s_f is the cross-section area of each DC coil turn. l_{f1} is the DC winding length for each turn. S_f is the DC winding slot area. k_{pff} is the DC winding packing factor.

Based on (3) and (4), (2) can be rewritten as,

$$IVR = \frac{1}{I_f N_{fc}} \times \frac{E_{pp1} S_f k_{pff}}{\rho l_{fc1}} \times 100\% \tag{5}$$

As shown in (3), E_{pp} will be lower with a lower N_{fc}. However, as shown in (5), due to a constant magnetomotive force (MMF) of DC winding $I_f N_{fc}$, IVR is constant with variation of N_{fc} as I_f changes inversely. Therefore, it is impossible to reduce IVR by changing N_{fc} when the DC winding MMF is fixed.

B. Mechanism

Due to the doubly-salient topology and magnetic gearing effect, there are abundant air-gap field harmonics in stator-excitation machines. Consequently, the open-circuit armature coil flux-linkage is not sinusoidal [see Fig. 6(a)], but suffers from many harmonics with various orders, as shown in Fig. 6(b). This is different from the conventional rotor-excitation synchronous machines [1], in which only odd harmonics will be generated in the open-circuit armature coil flux-linkage as there is no even field MMF. However, by appropriately connecting armature coils belong to the same phase to design the zero distribution factor for even harmonics, they can be eliminated in the open-circuit armature phase winding flux-linkage, Fig. 6(b), as analyzed in [19] for the 12-stator-pole PS-WFSF machines. Consequently, the open-circuit armature phase winding flux-linkage is more sinusoidal than those of the armature coils, as shown in Fig. 6(a).

Similar to open-circuit flux-linkage harmonics in armature coils, abundant harmonics will also be generated in the open-circuit coil f_1 flux-linkage ψ_{f1} due to the doubly-salient topology and magnetic gearing effect in stator-excitation machines, as shown in Fig. 7. As shown in Fig. 7(a), the only difference between the open-circuit DC coil flux-linkage waveforms for different coils is the phase angle, *i.e.* 30 electric degrees lag. Hence, they have the same harmonic spectrum as shown in Fig. 7(b). However, only the $6k^{th}$ (k=1,2,3…) harmonics remain in the open-circuit DC winding flux-linkage ψ_{DC}, as shown in Fig. 4(b) and hence the induced voltage in Fig. 5(b). The harmonic orders of the open-circuit DC winding flux-linkage ψ_f and hence the induced voltage E_f will be derived later.

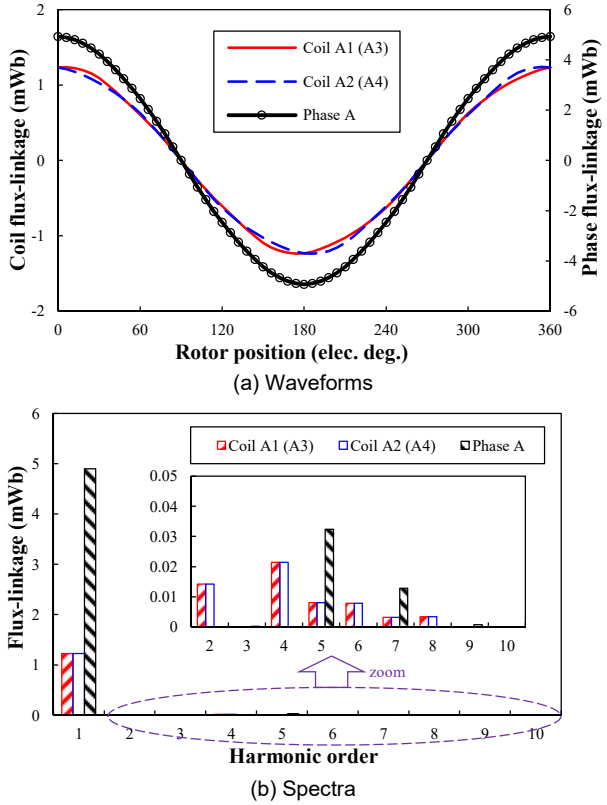

Fig. 6. Open-circuit armature coils A1, A2, A3, A4 and armature phase winding A flux-linkages in the 12/10-pole PS-WFSF machine (p_{cu}=60W).

As shown in Fig. 7(a), the open-circuit coil f_1 flux-linkage ψ_{f1} reaches the maximum and minimum values 26.05mWb and 23.43mWb when θ_e=120° and θ_e=300°, respectively. When θ_e=120°, as the flux of the tooth f_1 mainly short-circuits directly via rotor iron piece and the teeth f_2 and f_{12}, only crossing the inner air-gap, Fig. 8(a), the magnetic reluctance of ψ_{f1} is the smallest. However, when θ_e=300°, since the flux of the tooth f_1 mainly crosses both the inner and outer air-gaps to the outer stator armature teeth, Fig. 8(b), the magnetic reluctance of ψ_{f1} is the highest. Consequently, the average flux density of the tooth f_1 and hence ψ_{f1} reach the maximum and minimum values when θ_e=120° and θ_e=300°, respectively, as shown in Fig. 9. It is worth noting that the waveforms shown in Fig. 8 and Fig. 9 are for the practical machine with saturated lamination steel, not for that with linear limation steel.

However, it is worth noting that the pulsation of ψ_{f1} cannot be eliminated but even higher by using linear lamination steel, as shown in Fig. 7. The black solid line without marker in Fig. 7(a) and the blue bars in Fig. 7(b) are the waveform and spectra of the flux-linkage for DC coil f_1 in the 12/10-pole PS-WFSF machine with linear lamination steel. This proves that the pulsation of ψ_{f1} is not caused by the variation of the inner stator tooth saturation level, but caused by that of the equivalent

air-gap magnetic reluctance when the rotor is rotating.

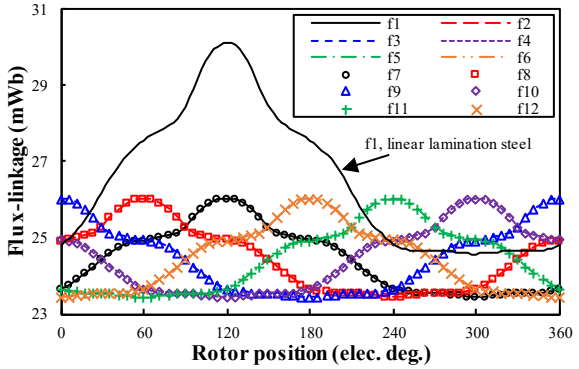

(a) Waveforms

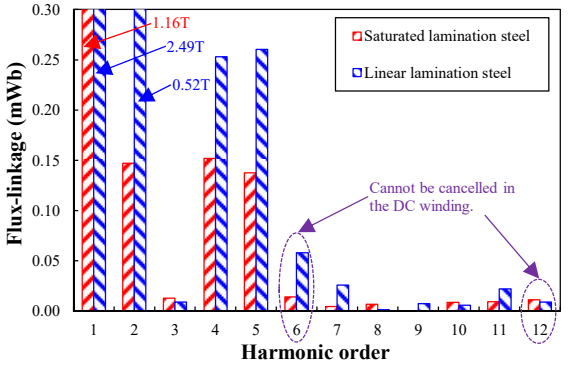

(b) Spectra for all coils

Fig. 7. Open-circuit DC coil flux-linkage in the 12/10-pole PS-WFSF machine (p_{cuf}=60W).

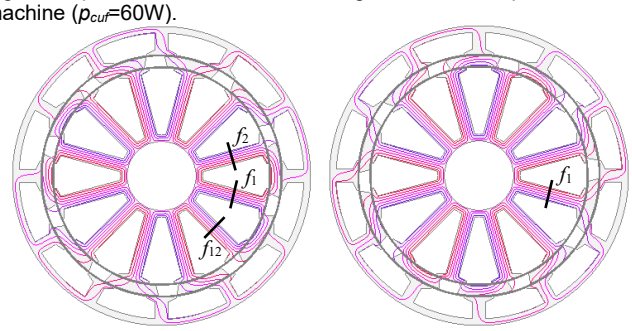

(a) Maximum (θ_e=120°) (b) Minimum (θ_e=300°)

Fig. 8. Flux path distribution of the 12/10-pole PS-WFSF machine when open-circuit ψ_{f1} is maximum and minimum (p_{cuf}=60W).

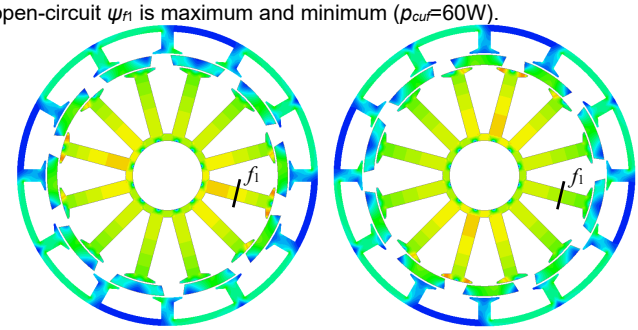

(a) Maximum (θ_e=120°) (b) Minimum (θ_e=300°)

Fig. 9. Flux density distributions of the 12/10-pole PS-WFSF machine when open-circuit ψ_{f1} is maximum and minimum (0-2T) (p_{cuf}=60W).

IV. Reduction of Open-circuit DC Winding Induced Voltage by Skewing

Skewing is a widely used method to reduce harmonics in both the conventional rotor-excitation machines, including cogging torque [24], back-EMF and hence torque ripple [25]. Although stator-excitation machines such as switched flux PM machines can have a sinusoidal phase back-EMF, it suffers from a high cogging torque and hence torque ripple, whilst skewing always reduces the cogging torque and hence torque ripple, as studied in [26]-[28].

In this section, harmonic orders of the open-circuit DC winding induced voltage is analytically derived firstly. Then, based on the analytically predicted harmonic orders, rotor skewing is adopted to reduce the open-circuit DC winding induced voltage, with optimal skewing angle derived.

C. Harmonic Orders

As shown in Fig. 7(b), many harmonics will be generated for the open-circuit DC coil f_1 flux-linkage ψ_{f1}, which can be expressed by a Fourier series as,

$$\psi_{f1} = \psi_0 + \sum_{i=1,2,3,\ldots}^{\infty} \psi_i \sin(iN_r\theta_m + \theta_i) \tag{6}$$

where ψ_0 is the average value. ψ_i and θ_i (i=1,2,3,…) is the i^{th} flux-linkage harmonic amplitude and initial phase, respectively. N_r is the rotor pole number. θ_m is the rotor mechanical position.

Similarly, for DC coil f_k (k=2,3,4,…,N_s), the flux-linkage ψ_{fk} can be expressed as,

$$\psi_{fk} = \psi_0 + \sum_{i=1,2,3,\ldots}^{\infty} \psi_i \sin[iN_r(\theta_m + \theta_{lk}) + \theta_i] \tag{7}$$

where θ_{lk} is the spatial electric lag angle of f_k to f_1. It can be expressed as,

$$\theta_{lk} = (k-1)\frac{2\pi}{N_s} \tag{8}$$

where N_s is the stator pole number.

Therefore, due to connecting in series, the DC winding flux-linkage ψ_f can be expressed as,

$$\begin{aligned}\psi_f &= \sum_{k=1,2,3,\ldots}^{N_s} \psi_{fk} \\ &= \sum_{k=1,2,3,\ldots}^{N_s} \sum_{i=0,1,2,\ldots}^{\infty} \psi_i \sin\left(\frac{2\pi N_r}{N_s}ik + N_r\theta_m i - \frac{2\pi N_r}{N_s}i + \theta_i\right) \\ &= \sum_{i=0,1,2,\ldots}^{\infty} \psi_i \left\{\cos\left[N_r\theta_m i - \frac{2\pi N_r}{N_s}i + \theta_i\right] \sum_{k=1,2,3,\ldots}^{N_s} \sin mik \right. \\ &\left. + \sin\left[N_r\theta_m i - \frac{2\pi N_r}{N_s}i + \theta_i\right] \sum_{k=1,2,3,\ldots}^{N_s} \cos mik \right\}\end{aligned} \tag{9}$$

where

$$m = \frac{2\pi N_r}{N_s}$$

The summation operator of sin mik and cos mik can be simplified as,

$$\sum_{k=1,2,3,\ldots}^{N_s} \sin mik = \frac{\sin\frac{N_s mi}{2}}{\sin\frac{mi}{2}} \sin\frac{(N_s+1)mi}{2} \tag{10}$$

and

$$\sum_{k=1,2,3,\ldots}^{N_s} \cos mik = \frac{\sin\frac{N_s mi}{2}}{\sin\frac{mi}{2}} \cos\frac{(N_s+1)mi}{2} \tag{11}$$

, respectively.

Therefore, based on (10) and (11), (9) can be rewritten as,

$$\psi_f = \sum_{i=0,1,2,\ldots}^{\infty} \psi_i \frac{\sin N_r i\pi}{\sin\frac{N_r i}{N_s}\pi} \sin\left(N_r i\theta_m + N_r i\pi - \frac{N_r i}{N_s}\pi + \theta_i\right) \tag{12}$$

As shown in (12), sin ($N_r i\pi$) is always 0. According to L'Hospital's Rule, only when sin ($N_r i\pi/N_s$) is 0, the corresponding i^{th} harmonic component of DC winding flux-linkage exists with,

$$\lim_{\substack{\sin N_r i\pi\to 0 \\ \sin\frac{N_r i}{N_s}\pi\to 0}} \frac{\sin N_r i\pi}{\sin\frac{N_r i}{N_s}\pi} = \lim_{\substack{\sin N_r i\pi\to 0 \\ \sin\frac{N_r i}{N_s}\pi\to 0}} N_s \frac{\cos N_r i\pi}{\cos\frac{N_r i}{N_s}\pi} = N_s \tag{13}$$

Therefore, it can be concluded from (12) that the open-circuit DC winding flux-linkage cycles per mechanical period $N_r i$ is,

$$N_r i = LCM(N_s, N_r) \tag{14}$$

where LCM is the least common multiple.

As well known, in the PS-WFSF machines, the relationship between rotor electric position θ_e and rotor mechanical positions θ_m is,

$$\theta_e = N_r \theta_m \tag{15}$$

Therefore, the open-circuit DC winding flux-linkage and hence the induced voltage cycles per electric period N_{pe} can be expressed as,

$$N_{pe} = \frac{LCM(N_s, N_r)}{N_r} \tag{16}$$

The equation (16) can be synthesized in TABLE III for the 12-stator-pole PS-WFSF machines having 10-, 11-, 13- and 14-rotor-pole rotors. As shown in TABLE III, N_{pe}=6 for the analyzed 12/10-pole PS-WFSF machine, *i.e.* the open-circuit DC winding flux-linkage is with harmonics of 6k (k=1,2,3,…). This can be verified by FE predicted harmonics as shown in Fig. 7(b). The equation (16) can also be verified by other stator/rotor-pole combinations, as evidenced in Fig. 10 for the 12-pole PS-WFSF machines having 11-, 13-, and 14-rotor-pole rotors. Due to higher harmonic orders, the 12/11- and 12/13-pole PS-WFSF machines have smaller open-circuit DC winding induced voltage than the 12/10- and 12/14-pole PS-WFSF machines.

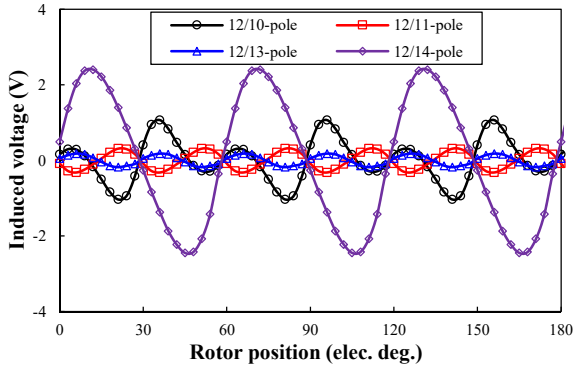

(a) Waveforms

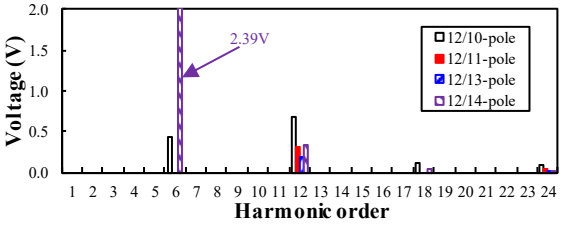

(b) Spectra

Fig. 10. Open-circuit DC winding induced voltages of 12-stator-pole PS-WFSF machines having 10-, 11-, 13- and 14-rotor-pole rotors at 400rpm.

TABLE III

ANALYTICAL PREDICTION OF N_{pe} AND θ_{sko}

Item	12-stator-pole PS-WFSF machines			
N_r	10	11	13	14
N_{pe}	6	12	12	6
θ_{sko}	°	60	30	30

D. Skewing

The open-circuit DC winding flux-linkage ψ_f can be expressed as the product of DC winding self-inductance L_f and DC winding current I_f,

$$\psi_f(\theta_e) = L_f(\theta_e) \times I_f(\theta_e) \tag{17}$$

Since the DC winding current I_f is constant, it can be concluded from (17) that the harmonics of the open-circuit DC winding flux-linkage ψ_f can be equivalent to those of the DC winding self-inductance L_f, which also has $N_{pe}k$ (k=1,2,3,…) orders. If the DC winding self-inductance harmonics can be reduced, the open-circuit DC winding flux-linkage vibration and hence the induced voltage will be suppressed. In this section, the rotor skewing shown in Fig. 11 is applied to reduce the DC winding self-inductance harmonics analytically and the optimal skewing angle to eliminate the harmonics is derived.

For the axially central cross-section of slice without skew, the corresponding self-inductance of DC winding L_{ffd} is,

$$L_{ffd} = \frac{1}{N}\left[L_{ff0} + \sum_{j=1,2,3,\ldots}^{\infty} L_{ffj}\cos(jN_{pe}\theta_e + \theta_{Lffj})\right] \tag{18}$$

where N is the number of step-skewing steps. L_{ff0} is the average value of DC winding self-inductance for the machine without rotor skewing. L_{ffj} and θ_{Lffj} are the amplitude and initial phase of the $(jN_{pe})^{th}$ DC winding self-inductance harmonic, respectively, for the machine without rotor skewing.

For the slice with skew angle of θ_s electric degrees, the corresponding self-inductance of DC winding can be given as,

$$L_{ffs} = \frac{1}{N}\left\{L_{ff0} + \sum_{j=1,2,3,\ldots}^{\infty} L_{ffj}\cos\left[jN_{pe}(\theta_e - \theta_s) + \theta_{Lffj}\right]\right\} \tag{19}$$

Therefore, when the continuous rotor skewing is applied with skewing angle θ_{sk}, the DC winding self-inductance is,

$$\begin{aligned} L_{ff} &= \frac{1}{\theta_{sk}}\int_{-\frac{\theta_{sk}}{2}}^{\frac{\theta_{sk}}{2}} L_{ff0} + \sum_{j=1,2,3,\ldots}^{\infty} L_{ffj}\cos\left[jN_{pe}(\theta_e - \theta_s) + \theta_{Lffj}\right] d\theta_s \\ &= L_{ff0} + \frac{2}{\theta_{sk}}\sum_{j=1,2,3,\ldots}^{\infty} \frac{L_{ffj}}{jN_{pe}} \sin\frac{jN_{pe}\theta_{sk}}{2} \cos\left(jN_{pe}\theta_e + \theta_{Lffj}\right) \end{aligned} \tag{20}$$

As shown in (20), the ratio of the $(jN_{pe})^{th}$ DC winding self-inductance harmonic with skewing angle θ_{sk} to that without

skewing, k_{skj}, can be given as,

$$k_{skj} = \frac{2}{jN_{pe}\theta_{sk}} \sin\frac{jN_{pe}\theta_{sk}}{2} \quad (21)$$

Based on (21), the relationships of open-circuit DC winding induced voltage 6th, 12th, 18th, and 24th harmonic magnitudes and the skewing angle θ_{sk} are shown in Fig. 12. As shown in Fig. 12, all k_{sk6}, k_{sk12}, k_{sk18} and k_{sk24} vary with skewing angle θ_{sk}. However, these open-circuit DC winding induced voltage harmonics can be reduced to zero in both the 12/10- and 12/14-pole PS-WFSF machines with θ_{sk}=60° and the 12/11- and 12/13-pole PS-WFSF machines with θ_{sk}=30°, although the open-circuit AC winding fundamental back-EMF and hence torque density will be slightly smaller due to skewing, *i.e.* 4.51% lower in 12/10- and 12/14-pole PS-WFSF machines and 1.14% lower in 12/11- and 12/13-pole PS-WFSF machines.

Moreover, as shown in (20) and (21), for minimizing all the $(jN_{pe})^{th}$ DC winding self-inductance harmonics with j=1,2,3,… and maintain the DC winding phase fundamental back-EMF, Fig. 12, the lowest optimal skew rotor angle θ_{sko} is given by,

$$\theta_{sko} = \frac{2\pi}{N_{pe}} \quad (22)$$

As shown in (22), if the skewing angle θ_{sk} is designated as $2\pi/N_{pe}$, all the DC winding self-inductance harmonics and hence the open-circuit DC winding induced voltage harmonics will be reduced to zero, as well as the peak to peak value of the open-circuit DC winding induced voltage E_{pp}. For the 12-stator-pole PS-WFSF machines having different rotor pole numbers, the optimal skewing angle θ_{sko} can be synthesized as shown in TABLE III.

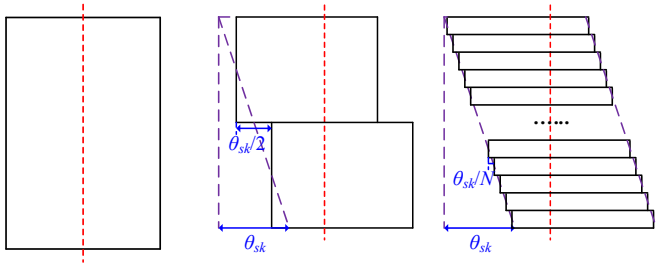

(a) Without skewing (b) 2-step skewing (c) *N*-step skewing

Fig. 11. Illustration of rotor iron piece skewing with skewing angle θ_{sk}.

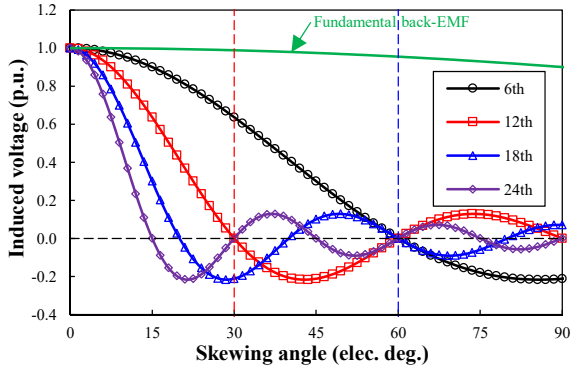

Fig. 12. Influence of skewing angle on the open-circuit DC winding induced voltages harmonics and AC winding phase fundamental back-EMF.

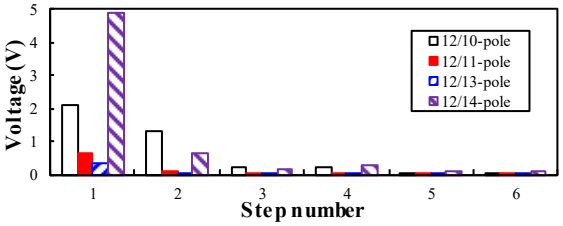

Fig. 13. 2D FE predicted influence of step-skewing number on peak to peak value of the open-circuit DC winding induced voltages (θ_{sk}=θ_{sko}, p_{cuf}=60W).

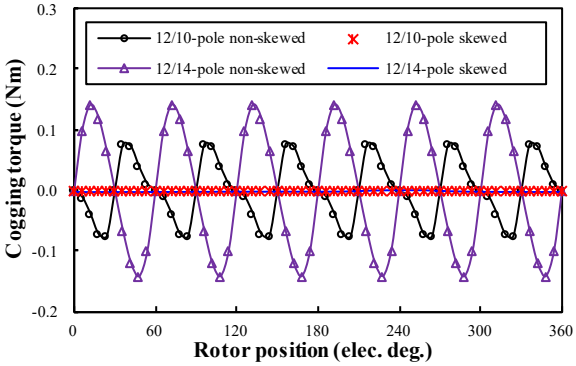

Fig. 14. Cogging torque waveforms of 12/10- and 12/14-pole PS-WFSF machines having non-skewed and skewed rotors (θ_{sk}=θ_{sko}, step number=5, p_{cuf}=60W).

The above analysis of skewing is based on continuous skewing. Here, the influence of skewing steps on the peak to peak value of the open-circuit DC winding induced voltage E_{pp} is investigated, when the optimal skewing angle θ_{sko} shown in (22) are applied. As shown in Fig. 13, when the step-skewing number is 5 and the skewing angle θ_{sk} is the optimal value θ_{sko} shown in TABLE III, the peak to peak value of the open-circuit induced voltage E_{pp} will be reduced by 98.59%, 95.20%, 94.13%, and 98.46% for the 12-stator-pole PS-WFSF machines with 10-, 11-, 13- and 14-rotor-pole rotors, respectively, whilst the AC winding phase fundamental back-EMFs can be maintained as high as 95.67% for the 10- and 14-rotor-pole machines and 98.91% for the 11- and 13-rotor-pole machines, respectively.

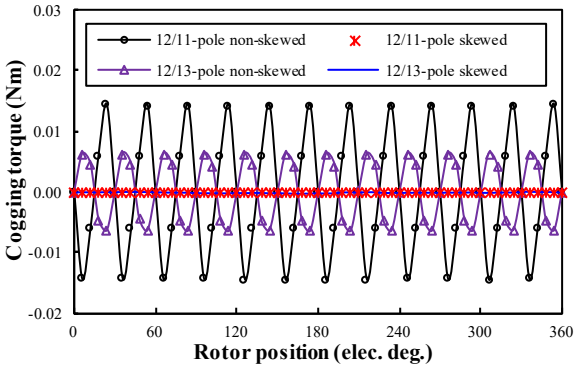

Fig. 15. Cogging torque waveforms of 12/11- and 12/13-pole PS-WFSF machines having non-skewed and skewed rotors (θ_{sk}=θ_{sko}, step number=5, p_{cuf}=60W).

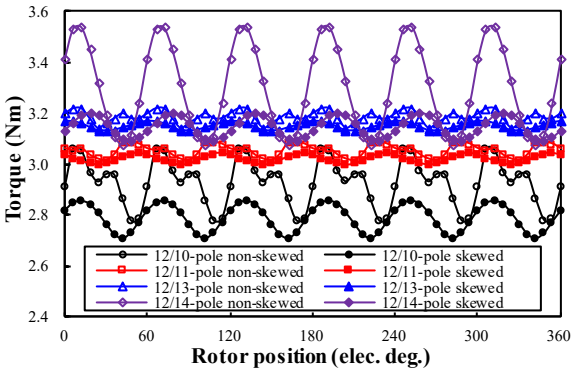

Fig. 16. Rated on-load electromagnetic torque waveforms of 12-stator-pole PS-WFSF machines having non-skewed and skewed rotors (θ_{sk}=θ_{sko}, step number=5, p_{cua}=p_{cuf}=60W, BLAC, i_d=0).

TABLE IV

CHARACTERISTICS OF COGGING TORQUE AND ON-LOAD ELECTROMAGNETIC TORQUE

Item	Unit	12-stator-pole PS-WFSF machines							
N_r	-	10		11		13		14	
θ_{sk}	°	0	60	0	30	0	30	0	60
T_{cog}	Nm	154.76	0.39	28.82	0.06	12.72	0.07	283.02	0.60
T_{avg}	Nm	2.93	2.79	3.05	3.02	3.19	3.15	3.30	3.15
T_{rip}	%	9.47	5.20	2.21	1.41	2.51	1.27	14.12	3.46

As shown in Fig. 14, Fig. 15 and TABLE IV, the cogging torque peak-to-peak value T_{cog} will also be reduced by applying a step skewing [29] with θ_{sk}=θ_{sko} and a step number=5, i.e. 99.75%, 99.80%, 99.42% and 99.79% for the 12-stator-pole PS-WFSF machines with 10-, 11-, 13- and 14-rotor-pole rotors, respectively. However, the torque ripple reduction is only 45.08%, 36.23%, 49.33% and 75.50%, respectively, as shown in Fig. 16 and TABLE IV, since the equivalent current angle of the electromagnetic torque waveforms for sub-machines are different [30]. As shown in Fig. 16 and TABLE IV, the average electromagnetic torque is also reduced by 4.77%, 1.09%, 1.11% and 4.68%, respectively, due to a smaller fundamental AC winding phase back-EMF. The torque ripple T_{rip} in TABLE IV is defined as,

$$T_{rip} = \frac{T_{max} - T_{min}}{T_{avg}} \times 100\% \quad (23)$$

where T_{max}, T_{min} and T_{avg} are the maximum, minimum and average values of electromagnetic torque.

V. EXPERIMENTAL VALIDATION

In this section, to validate the foregoing analytical and FE analyses, the 12/10-pole prototypes with skewed rotor and non-skewed rotor with θ_{sk}=60° are built and tested. The photos of the prototypes are shown in Fig. 17. For easing the rotor manufacturing, a 0.5mm thick iron flux-bridge is introduced adjacent to the outer air-gap to connect the rotor iron pieces.

It is worth noting that not the open-circuit DC winding induced voltage but that of the DC coil 2 is measured in this section to validate the FE analysis, since the influence of the DC current supply on the measured voltage cannot be separated if the DC winding is loaded. Alternatively, only DC coils 1, 3, 5, 7, 9 and 11 are loaded with 2I_f=7.2A, whilst coils 2, 4, 6, 8, 10 and 12 are open-circuit, resulting in a same DC winding MMF as the condition that all DC coils are loaded with I_f=3.6A. The DC current supply has no influence on the open-circuit induced voltage of the DC coil 2 as it is open-circuit.

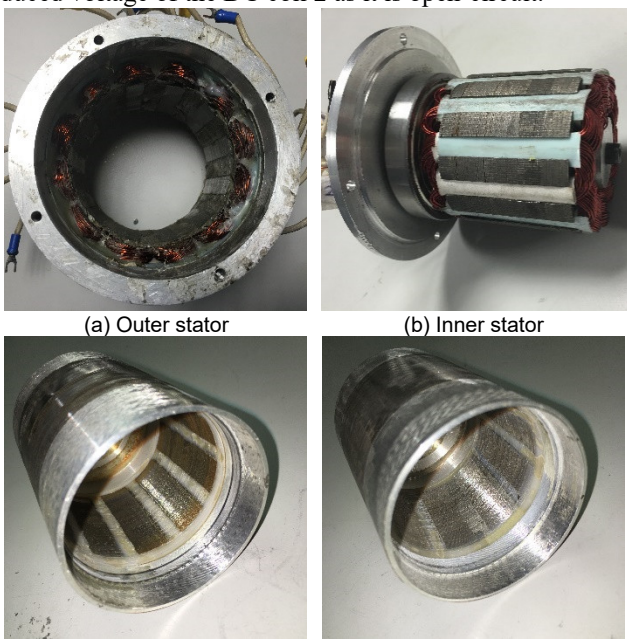

(a) Outer stator (b) Inner stator

(c) Non-skewed rotor (d) Skewed rotor with θ_{sk}=60°

Fig. 17. Photos of the 12/10-stator/rotor-pole PS-WFSF machine prototypes with non-skewed and skewed rotors.

The measured open-circuit DC coil 2 induced voltage and phase A back-EMF at 400rpm are shown in Fig. 18. As shown in Fig. 19, in both machines with non-skewed and skewed rotors, both the measured DC coil 2 induced voltages and phase A back-EMFs are smaller than the 2-D FE predicted results due to end-effect. However, the measured results agree well with the 3D FE predicted values.

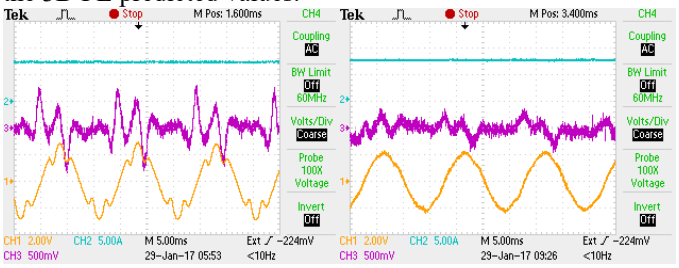

(a) Non-skewed rotor (b) Skewed rotor

Fig. 18. Measured phase A back-EMF (CH1), DC winding current (CH2) and open-circuit DC coil 2 induced voltage (CH3) at 400rpm (I_f=3.6A).

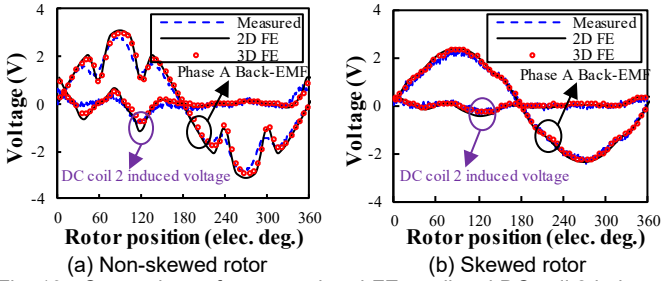

(a) Non-skewed rotor (b) Skewed rotor

Fig. 19. Comparison of measured and FE predicted DC coil 2 induced voltage and phase A back-EMF waveforms at 400rpm (I_f=3.6A).

Based on the measured open-circuit DC coil 2 induced voltages shown in Fig. 18, those of the DC winding are calculated based on Fig. 7(a) and comparatively shown in Fig. 20. As shown in Fig. 20, the dominant 6th harmonic of the open-circuit DC winding induced voltage harmonic can be

reduced by 44.14% by rotor skewing, i.e. 0.27V and 0.12V, respectively, although the $6k$ (k=1,2,3,…) harmonics of the open-circuit DC winding induced voltage cannot be reduced to zero in the prototype with skewed rotor due to the manufacturing error.

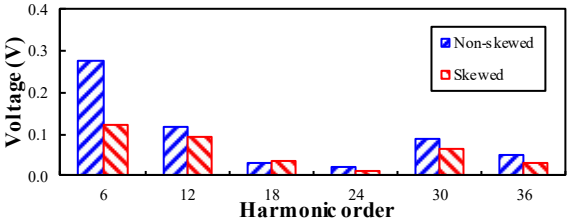

Fig. 20. Comparison of calculated open-circuit DC winding induced voltages harmonics based on the measured open-circuit DC coil 2 induced voltages at 400rpm (I_f=3.6A).

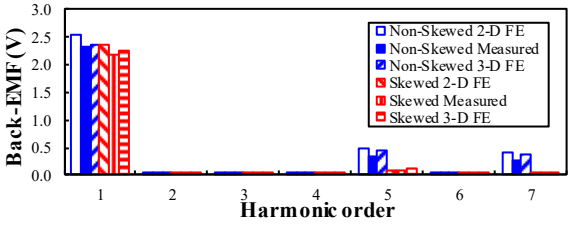

Fig. 21. Comparison of calculated open-circuit phase A back-EMF harmonics at 400rpm (I_f=3.6A).

As shown in Fig. 21, the 5th and 7th harmonics of the open-circuit phase A back-EMF are reduced due to rotor skewing with θ_{sk}=60° although the fundamental value is also slightly reduced. As shown in Fig. 22, when the currents of phases A, B and C match I_a=-2I_b=-2I_c, the static torques of both prototypes predicted by FE can be validated by the measured values. As shown in Fig. 23, although the measured cogging torque is slightly distorted and higher than FE predicted results due to manufacturing, it can also be effectively reduced by rotor skewing with θ_{sk}=60°. The cogging torque is measured based on the method used in [31].

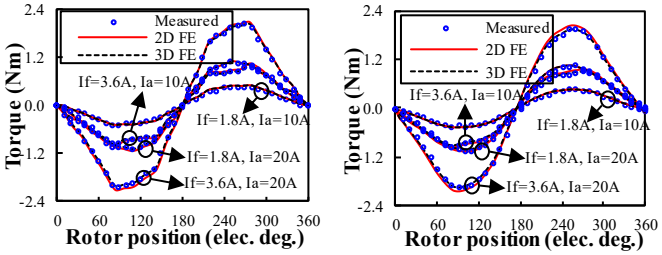

(a) Non-skewed rotor (b) Skewed rotor

Fig. 22. Comparison of measured and FE predicted static torque waveforms (I_f=3.6A, I_a=-2I_b=-2I_c).

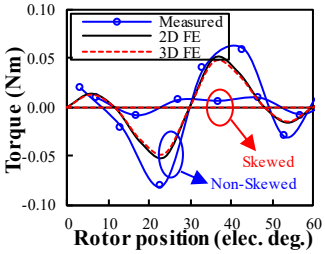

Fig. 23. Comparison of measured and FE predicted cogging torque waveforms (I_f=3.6A).

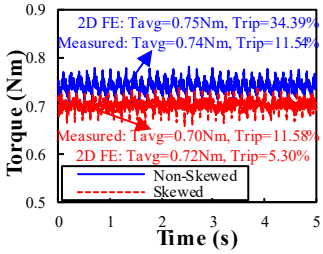

Fig. 24. Comparison of measured and FE predicted shaft torque waveforms at 400rpm (I_f=3.6A, BLAC, i_d=0, i_q=8A).

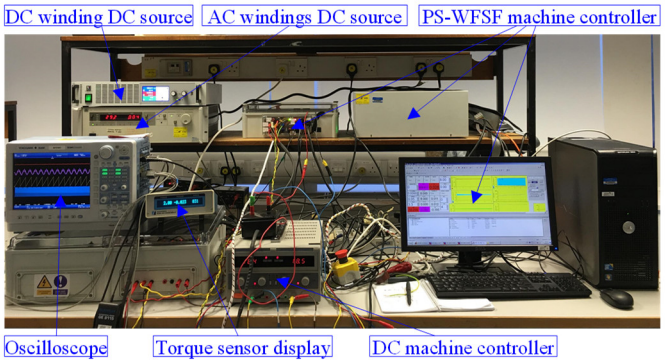

(a) Electrical components

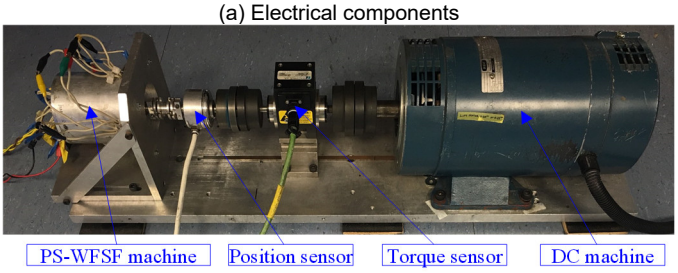

(b) Mechanical components

Fig. 25. Experiment platform of the PS-WFSF machine.

The average values of shaft torque waveforms at 400rpm of both prototypes can also be validated by the measured values and the results show that the average torque is reduced due to rotor skewing, as shown in Fig. 24. Although the FE results show that the electromagnetic torque ripple can be reduced from 34.39% to 5.30% by using skewed rotor, the measured shaft torque ripples are similar due to the harmonic of which the frequency is equal to the fundamental mechanical frequency of the prototype, i.e. 6.67Hz. This is caused by the imperfect connection among mechanical components shown in Fig. 25(b), i.e. axial unalignment. As for the shaft torque waveforms shown in Fig. 24, the excitations of both DC winding and AC windings of the PS-WFSF prototypes are realized by H-bridge.

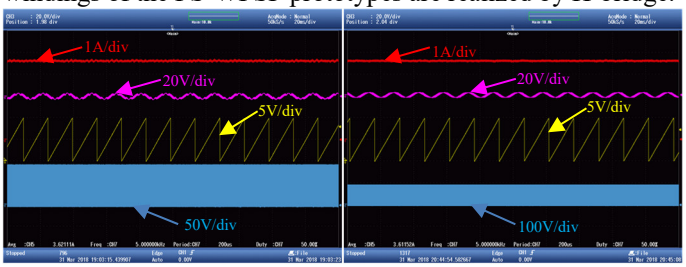

(a) Non-skewed, H-bridge (b) Skewed, H-bridge

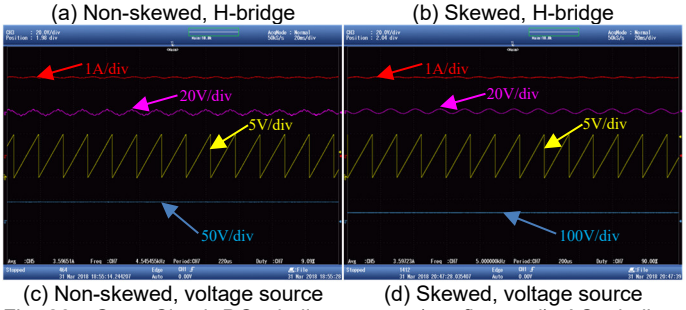

(c) Non-skewed, voltage source (d) Skewed, voltage source

Fig. 26. Open-Circuit DC winding current (top first, red), AC winding phase A back-EMF (top second, pink), rotor position (top third, yellow) and DC winding voltage (top fourth, blue) at 400rpm when the DC winding is supplied by H-bridge or voltage source (I_f=3.6A).

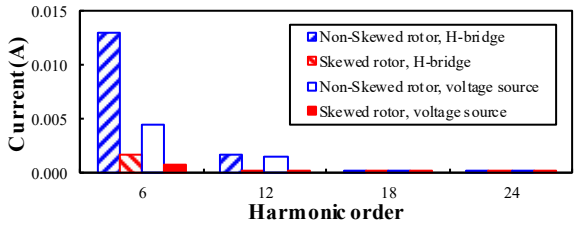

Fig. 27. Comparison of the harmonics of open-circuit DC winding currents at 400rpm (p_{cuf}=60W).

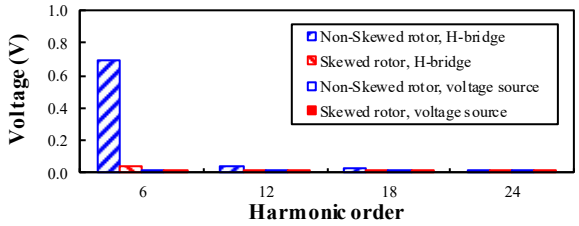

Fig. 28. Comparison of the harmonics of open-circuit DC winding voltages at 400rpm(p_{cuf}=60W).

The impact of open-circuit induced voltage on DC winding circuit is also evaluated on the prototypes by measuring and comparing the open-circuit DC winding current and voltage at 400rpm when the DC winding voltage is supplied by H-bridge or constant voltage source, as shown in Fig. 26. When the DC winding voltage is supplied by a constant voltage source, the constant voltage is set as the rated DC winding resistance voltage drop to achieve I_f=3.6A, i.e. the rotor is standstill. When the DC winding voltage is supplied by the H-bridge, a closed-loop DC winding current control is implemented with a reference value I_f*=3.6A. As shown in Fig. 27 and Fig. 28, both the DC winding current and voltage suffer from the 6th harmonics. However, there are less 6th harmonics in the DC winding current and voltage when it is supplied a constant voltage source. Moreover, it can be observed that when the DC winding is supplied by the H-bridge, not only a constant DC winding resistance voltage but also a 6th harmonic voltage are required to balance the DC winding induced voltage. However, both of them can be effectively reduced by rotor skewing.

VI. Discussion and Conclusion

In this paper, open-circuit DC winding induced voltage in the PS-WFSF machine is analysed. It is found that the open-circuit DC winding induced voltage is caused by the variable air-gap magnetic reluctance when the rotor is rotating, which can be regarded as the harmonics of DC winding self-inductance. Harmonic orders of the open-circuit DC winding induced voltage is analytically derived and verified by FE results, *i.e.* $LCM(N_s,N_r)/N_r$. It is also found that skewing can reduce the open-circuit DC winding induced voltage to zero, although the open-circuit AC winding fundamental back-EMF and hence the torque density will be slightly smaller. The 12/10-pole prototype with skewed and non-skewed rotors is built and tested to verify the analytical and FE results. The analysis in this paper is also applicable for other WFSF machines with different topologies and sizes.

At on-load condition, the DC winding induced voltage consists of two components, i.e. not only the open-circuit one but also that caused by armature reaction. As for reduction approaches, apart from skewing and optimization of stator/rotor-pole combination, some others approaches used to reduce cogging torque [29] and torque ripple [32] in PM machines may also be effective to reduce the DC winding induced voltages in WFSF machines, e.g. introducing notches in the stator teeth which are wound by DC coils, and shaping the surface of these teeth. Future works can be carried out to extend the analysis in this paper to the on-load DC winding induced voltage and the corresponding reduction methods.

References

[1] Z. Q. Zhu, and D. Howe, "Electrical machines and drives for electric, hybrid and fuel cell vehicles," *Proc. IEEE*, vol. 95, no. 4, pp. 746-765, Apr. 2007.

[2] I. Boldea, L. N. Tutelea, L. Parsa, and D. Dorrell, "Automotive electric propulsion systems with reduced or no permanent magnets: an overview," *IEEE Trans. Ind. Electron.*, vol. 61, no. 10, pp. 5696-5711, Oct. 2014.

[3] S. Williamson, A. Smith, M. Begg, and J. Smith, "General techniques for the analysis of induction machines using finite elements," in *Proc. Int. Conf. Evol. Modern Aspect Induction Motors*, Turin, Italy, Jul. 1986, pp. 389-395.

[4] K. Kiyota, T. Kakishima, and A. Chiba, "Comparison of test result and design stage prediction of switched reluctance motor competitive with 60-kW rare-earth PM motor," *IEEE Trans. Indus. Electron.*, vol. 61, no. 10, pp. 5712-5721, Oct. 2014.

[5] M. L. Bash, and S. D. Pekarek, "Modeling of salient-pole wound-rotor synchronous machines for population-based design," *IEEE Trans. Energy Convers.*, vol. 26, no. 2, pp. 381-392, Jun. 2011.

[6] C. Pollock and M. Wallace, "The flux switching motor, a DC motor without magnets or brushes," in *Conf. Rec. IEEE IAS Annu. Meeting*, 1999, vol. 3, pp. 1980-1987.

[7] Y. Tang, J. J. H. Paulides, T. E. Motoasca, and E. A. Lomonova, "Flux switching machine with DC excitation," *IEEE Trans. Magn.*, vol. 48, no. 11, pp. 3583-3586, Nov. 2012.

[8] U. B. Akuru, and M. J. Kamper, "Formulation and multiobjective design optimization of wound-field flux switching machines for wind energy drives," *IEEE Trans. Indus. Electron.*, vol. 65, no. 2, pp. 1828-1836, Feb. 2018.

[9] S. M. Yang, J. H. Zhang, and J. Y. Jiang, "Modeling torque characteristics and maximum torque control of a three-phase, DC-excited flux-switching machine," *IEEE Trans. Magn.*, vol. 52, no. 7, Jul. 2016, Art. ID 8104204.

[10] B. Gaussens, E. Hoang, O. de la Barrière, J. Saint-Michel, P. Manfe, M. Lécrivain, and M. Gabsi, "Analytical armature reaction field prediction in field-excited flux-switching machines using an exact relative permeance function," *IEEE Trans. Magn.*, vol. 49, no. 1, pp. 628-641, Jan. 2013.

[11] J. T. Chen, Z. Q. Zhu, S. Iwasaki, and R. Deodhar, "Low cost flux-switching brushless AC machines," *Proc. Conf. Veh. Pow. Prop.*, Lille, France, 2010, pp. 1-6.

[12] Y. Wang, and Z. Deng, "A position sensorless method for direct torque control with space vector modulation of hybrid excitation flux-switching generator," *IEEE Trans. Energy Convers*, vol. 27, no. 4, pp. 912-921, Dec. 2012.

[13] Z. Q. Zhu, and X. Liu, "Novel stator electrically field excited synchronous machines without rare-earth magnet," *IEEE Trans. Magn.*, vol. 51, no. 4, Apr. 2015, Art. ID 8103609.

[14] E. Sulaiman, T. Kosaka, and N. Matsui, "Design study and experimental analysis of wound field flux switching motor for HEV applications," in *Proc. IEEE Inter. Conf. Elec. Mach.*, Marseille, France, Sep. 2012, pp. 1269-1275.

[15] T. Raminosoa, *A. M. El-Refaie, D. Pan, K. K. Huh, J. P. Alexander, K. Grace, S. Grubic, S. Galioto, P. B. Reddy, and X. Shen*, "Reduced rare-earth flux-switching machines for traction applications," *IEEE Trans. Ind. Appl.*, vol. 51, no. 4, pp. 2959-2971, Jul.-Aug. 2015.

[16] T. Fukami, Y. Matsuura, K. Shima, M. Momiyama, and M. Kawamura, "A multi-pole synchronous machine with nonoverlapping concentrated armature and field winding on the stator," *IEEE Trans. Ind. Electron.*, vol. 59, no. 6, pp. 2583-2591, Jun. 2012.

[17] A. Zulu, B. Mecrow, and M. Armstrong, "A wound-field three-phase flux-switching synchronous motor with all excitation sources on the

stator," *IEEE Trans. Ind. Appl.*, vol. 46, no. 6, pp. 2363-2371, Nov./Dec. 2010.
[18] Z. Q. Zhu, Y. J. Zhou, and J. T. Chen, "Electromagnetic performance of nonoverlapping stator wound field synchronous machine with salient pole rotor," *IEEE Trans. Magn*., vol. 51, no. 11, Nov. 2015, Art. ID 8110104.
[19] Z. Q. Zhu, Z. Z. Wu, D. J. Evans, and W. Q. Chu, "A wound field switched flux machine with field and armature windings separately wound in double stators," *IEEE Trans. Energy Convers*, vol. 30, no. 2, pp. 772-783, Jun. 2015.
[20] Z. Z. Wu, Z. Q. Zhu, J. C. Mipo, and P. Farah, "Design and analysis of a partitioned stator wound field switched flux machine for electric vehicle," *in Proc. of ICEMS 2016*, Chiba, Japan, 2016, pp. 1-6.
[21] Oak Ridge National Laboratory, "Evaluation of the 2010 Toyota Prius hybrid synergy drive system", 2011.
[22] C. Yu, and S. Niu, "Development of a magnetless flux switching machine for rooftop wind power generation," *IEEE Trans. Energy Convers.*, vol. 30, no. 4, pp. 1703-1711, Dec. 2015.
[23] S. X. Niu, K. T. Chau, and J. Z. Jiang, "Analysis of eddy-current loss in a double-stator cup-rotor PM machine," *IEEE Trans. Magn.*, vol. 44, no. 11, pp. 4401-4404, Nov. 2008.
[24] T. Li, and G. Slemon, "Reduction of cogging torque in permanent magnet motors," *IEEE Trans. on Magn.*, vol. 24, no. 6, pp. 2901-2903, Nov 1988.
[25] T. Sebastian, and V. Gangla, "Analysis of induced EMF waveforms and torque ripple in a brushless permanent magnet machine," *IEEE Trans. Ind. Appl.*, vol. 32, no. 1, pp. 195-200, Jan./Feb. 1996.
[26] W. Fei, P. C. K. Luk, and J. Shen, "Torque analysis of permanent-magnet flux switching machines with rotor step skewing," *IEEE Trans. on Magn.*, vol. 48, no. 10, pp. 2664-2673, Oct. 2012.
[27] N. Bianchi, and S. Bolognani, "Design techniques for reducing the cogging torque in surface-mounted PM motors," *IEEE Trans. Ind. Appl.*, vol. 38, no. 5, pp. 1259-1265, Sep./Oct. 2002.
[28] Z. Q. Zhu, S. Ruangsinchaiwanich, and D. Howe, "Synthesis of cogging-torque waveform from analysis a single stator slot," *IEEE Trans. Magn*., vol. 45, no. 4, pp. 2023-2031, Apr. 2009.
[29] N. Bianchi, and S. Bolognani, "Design techniques for reducing the cogging torque in surface-mounted PM motors," *IEEE Trans. Ind. Appl*., vol. 38, no. 5, pp. 1259-1265, Sep./Oct. 2002.
[30] W. Q. Chu, and Z. Q. Zhu, "Reduction of on-load torque ripples in permanent magnet synchronous machines by improved skewing," *IEEE Trans. on Magn.*, vol. 49, no. 7, pp. 3822-3825, Jul. 2013.
[31] Z. Q. Zhu, "A simple method for measuring cogging torque in permanent magnet machines," *in Proc. of IEEE Power & Energy Society General Meeting*, 2009, pp. 1-4.
[32] T. M. Jahns, and W. L. Soong, "Pulsating torque minimization techniques for permanent magnet AC motor drives-a review," *IEEE Trans. Indus. Electron.*, vol. 43, no. 2, pp. 321-330, Apr. 1996.

Z. Z. Wu (S'15-M'18) received the B.Eng. and M.Sc. degrees in electrical engineering from Southeast University, Nanjing, China, in 2010 and 2013, respectively, and the Ph.D. degree in electrical and electronic engineering from The University of Sheffield, Sheffield, U.K., in January 2017.

Since January 2017, he has been with Warwick Manufacturing Group (WMG), The University of Warwick, Coventry, U.K., where he is currently a research fellow. His major research interests include the analysis, design, control and manufacturing of synchronous machines and magnetic gear for electrical vehicle and wind power generation applications.

Z. Q. Zhu (M'90–SM'00–F'09) received the B.Eng. and M.Sc. degrees in electrical and electronic engineering from Zhejiang University, Hangzhou, China, in 1982 and 1984, respectively, and the Ph.D. degree in electrical and electronic engineering from The University of Sheffield, Sheffield, U.K., in 1991.

Since 1988, he has been with The University of Sheffield, where he is currently a Research Chair of the Royal Academy of Engineering/Siemens with the Department of Electronic and Electrical Engineering and the Head of the Electrical Machines and Drives Research Group. His current major research interests include the design and control of permanent-magnet brushless machines and drives for applications ranging from automotive through domestic appliance to renewable energy. He is a Fellow of the Royal Academy of Engineering.

C. Wang received the B.Eng. and M.Sc. degrees in electrical engineering from Hefei University of Technology, Hefei, China, in 2008 and 2011, respectively. He is currently working toward the Ph.D. degree in electronic and electrical engineering from the University of Sheffield, Sheffield, U.K.

From 2011 to 2015, he was an Engineer at Midea Welling Motor Technology Company, Ltd., Shanghai, China. His research interests include the control of electric drives.

J. C. Mipo received the Ph.D. degree in electrical engineering from Pierre-and-Marie-Curie University, Paris, France.

Since 1998, he has been with Valeo Engine and Electrical Systems, Creteil, France, where he is currently an Advanced Technical Manager.

S. Personnaz received the Ph.D. degree in electric engineering from the Laboratoire d'Electrotechnique de Grenoble, Grenoble, France, in 1992.

Since 2017, she has been with Valeo Engine and Electrical Systems, Creteil, France, where she is currently the PES Electrotechnical Director, one of Powertrain Electrical System core activity. She leads the team of electric machine designers for the low voltage applications.

P. Farah received the Ph.D. degree in electrical engineering from the Institute National Polytechnique de Grenoble, France, in 1995.

From 2013 to 2016, he was with Valeo Engine and Electrical Systems, Creteil, France, as the Director of the Electromagnetic Design Group.